Nonlinear Infrared Spectroscopy of Protein Conformational Change during Thermal Unfolding

Hoi Sung Chung, Munira Khalil,[†] and Andrei Tokmakoff*

Department of Chemistry, Massachusetts Institute of Technology, Cambridge, Massachusetts 02139

Femtosecond two-dimensional infrared (2D IR) spectroscopy, dispersed vibrational echo (DVE) spectroscopy, and dispersed pump−probe (DPP) spectroscopy of the amide I vibrations are used to follow the thermal denaturing of ribonuclease A. Each experiment measures a spectrum with features that reflect vibrational couplings between amide I transitions of the protein backbone and is therefore more sensitive to protein conformation than traditional FTIR spectroscopy. As the temperature is raised, 2D IR spectra show the disappearance of cross peaks between two vibrational transitions arising from antiparallel β-sheet structure as well as the blue shift to a diagonally elongated inhomogeneous spectrum. DVE and DPP spectra can be related to projections of the complex 2D IR correlation spectrum and also show clear signatures of β-sheet structure in the native state. Singular value decomposition of the nonlinear spectra reveal a pretransition at 47 °C that precedes the melting of β sheets in the primary denaturing transition at 65 °C. Residual secondary structure is observed in the thermally denatured state. These experiments suggest that nonlinear infrared spectroscopy is an effective probe of protein conformation that can be used to probe the equilibrium thermodynamics and nonequilibrium kinetics and dynamics of protein folding.

I. Introduction

From one perspective, the experimental study of protein folding involves the characterization of a heterogeneous ensemble of structures over time scales ranging from picoseconds to seconds. The vast range of length and time scales involved makes the direct observation of structural coordinates difficult and ensures that no single experimental technique can capture structural changes at high spatial resolution in solution over all time scales.[1−4] Multidimensional nuclear magnetic resonance (NMR) spectroscopy provides an atomic-level structural tool in solution, but its use for following the folding of proteins has been limited to time scales of seconds.[5] Advances in time-resolved X-ray diffraction promises to reveal the details of time-dependent structural change with atomic resolution in crystals,[6,7] and X-ray scattering methods in solution give more limited structural information.[8] The inherently fast time scales of high-frequency spectroscopic techniques in the optical and infrared regimes make them appealing tools, although they lack the atomistic detail of X-ray and NMR. Nonetheless, time-resolved fluorescence,[3,9,10] infrared,[11−13] Raman,[14] and UV circular dichroism[15−20] have been used with considerable success to reveal folding and denaturing processes in proteins on picosecond to millisecond time scales.

Of these latter methods, infrared spectroscopy is appealing because of its structural sensitivity to nuclear degrees of freedom, its picosecond intrinsic measurement time scale, and no requirement of chromophores or prosthetic groups. IR spectroscopy is sensitive to protein structure through vibrational resonances arising from the polypeptide backbone or side chains. The protein structure, local interactions such as hydrogen

bonding, and the electrostatic and mechanical couplings between its various vibrational degrees of freedom determine the resonance frequencies observed in the infrared spectrum. Consequently, the infrared spectrum can be used to reveal structural information about the protein, yet even with these potential advantages, traditional protein IR spectroscopy is a largely qualitative method for two primary reasons. First, IR spectra of proteins are generally broad and featureless because of overlapping contributions from many oscillators, making assignment and modeling ambiguous. Also, the quantitative relationships between vibrational resonance frequencies and structure, as encoded in the various couplings between vibrations, are not understood well enough to allow a clear interpretation. However, these topics are presently receiving considerable attention, and there is a rapid pace of development from both the experimental and theoretical perspectives.[21−30]

Nonlinear IR spectroscopies offer the possibility of overcoming some of the complications with traditional linear IR spectroscopy. Rather than just revealing a sum of fundamental transitions for the vibrational eigenstates of the system, third-order nonlinear experiments with femtosecond IR pulses drive the system with three sequential electric field interactions through multiple vibrational states. As a result, they can be designed to probe vibrational couplings, the relative orientation between transition dipoles, inhomogeneous broadening or heterogeneity in the ensemble, and interactions that lead to correlated vibrational frequency shifts.[31] Perhaps the most general and powerful method is two-dimensional infrared (2D IR) spectroscopy, which in a manner analogous to 2D NMR spectra spreads vibrational resonances over two frequency dimensions, revealing vibrational couplings through the formation of cross peaks.[26,31,32] However, simpler nonlinear IR experiments that are derived from the same nonlinear response function, such as the frequency-dispersed pump probe (DPP)

Conformational Change during Thermal Unfolding

J. Phys. Chem. B, Vol. 108, No. 39, 2004 **15333**

and dispersed vibrational echo (DVE),[33−35] should also have considerable power for revealing resonances hidden in traditional IR spectra.

The investigations described in this paper aim to demonstrate the considerable power of 2D IR, DPP, and DVE experiments as structurally sensitive methods for the study of protein folding and denaturing. We focus on how these nonlinear experiments reveal transitions not seen in congested protein IR spectra and how they characterize changes in conformation and loss of secondary structure between the compact native state and a disordered, thermally denatured state. Our investigations probe the amide I vibrations of the protein backbone, which result from the couplings between the individual amide vibrations of each peptide unit along the protein backbone. For a single peptide unit, the amide I vibration is primarily the C=O stretching motion with some contribution from CN stretching and the CCN deformation motions.[22] The amide I IR spectrum is sensitive to conformation through the vibrational couplings between the amide I vibrations of each peptide unit and the amide frequency shifts due to hydrogen bonding.[36] Whether in small peptides[23,29,30,32,37−40] or proteins,[21,41,42] this leads to frequency shifts and absorption patterns characteristic of local or larger scale conformation. In proteins, correlations have been established linking secondary structural elements with characteristic amide I absorption frequencies, for instance, α-helices, ~1650 cm^{-1}; β sheets, ≤1640 and ≥1680 cm^{-1}; and random coils, ~1640−1650 cm^{-1}.[43−46] These can, to a first approximation, be accounted for by electrostatic couplings between oscillators in a given secondary structural configuration.[41] Nonetheless, testing and application of models for couplings in proteins is of limited use in traditional IR spectroscopy because of congestion and inhomogeneous broadening.

The present results build on our recent theoretical and experimental efforts to understand how 2D IR spectroscopy can be used to overcome some of the disadvantages of traditional IR spectroscopy of protein amide I transitions. As a particular strength, we have found that 2D IR spectroscopy is sensitive to the details of antiparallel β-sheet secondary structure.[47,48] FTIR spectra of proteins and peptides with antiparallel (AP) β sheets show a pair of transitions, a strong one (α−) that lies between 1610 and 1640 cm^{-1} and a weak one (α+) between 1680 and 1700 cm^{-1}.[22,41,47,49] We have found that the two amide I features are revealed in 2D IR spectra of AP β-sheet-containing proteins through the formation of a cross peak between the α− and α+ transitions.[47] For large ordered β sheets, such as those found in poly-L-lysine at high pH, the 2D IR correlation spectrum shows distinct cross peaks between the two amide I resonances.[48] These features are retained in the 2D IR spectra of proteins with AP β sheets even when other secondary structures are present, although it appears considerably different. Because the splitting between the α+ and α− resonances is sensitive to the strength of amide I couplings, the size and geometry of the sheet, and structural or energetic disorder associated with the peptide units within the sheet, these transitions become inhomogeneously broadened in proteins. As a result, we find that for proteins interference effects between the diagonal and cross peaks arising from inhomogeneous α− and α+ transitions stretch the cross peaks and, when combined with elongated resonances from additional amide transitions along the diagonal, leads to a characteristic "Z"-shaped pattern for the amide I region in the 2D IR spectrum.[48]

In the experiments below, we use linear and nonlinear IR experiments to characterize the conformational changes that accompany the thermal denaturing and folding of ribonuclease

A (RNase A), with particular emphasis on the changes associated with β sheets. RNase A is a 124-residue enzyme that catalyzes the degradation of RNA. An abundance of detailed structural information and studies of folding exist for RNase A, making it an excellent model system to test new experimental methods for probing the structural dynamics of protein folding and unfolding. The main secondary structural elements of RNase A include a V-shaped antiparallel β sheet with three strands on one side and four on the other and three helices.[50,51] Previous IR, Raman, and UV CD studies have shown that the thermal denaturation of RNase A is a reversible process with a melting temperature of approximately 63 °C and that this melting involves the loss of β-sheet content.[52−56] Previous studies have shown that the thermally denatured states of RNase A retain a sizable amount of nonrandom structure.[54,57−59] This is not altogether surprising because the disulfide bonds, which hold the protein together, remain intact at high temperatures.[60] This view is supported by the measurement of the radius of gyration of the thermally denatured states, which increases from 20 to 30 Å under reducing conditions.[61] However, the comparison of the FTIR spectra of thermally and chemically denatured protein has shown that this residual structure is not same as the native structure.[62] Recent FTIR and CD measurements have revealed that the folding/unfolding of RNase A is not a simple two-state process but also shows a pretransition around 47 °C.[52] It has been suggested that the pretransition involves the unwinding of the helix at the N terminus along with the destabilization of the β strand involving residues 43−49.

Two-dimensional IR experiments are used to follow the denaturing of the protein, showing the loss of cross peaks and other spectral features that form a Z-shaped contour profile characteristic of AP β sheets. This indicates a disruption of interstrand amide I couplings that is consistent with the melting of the β sheet. We also show that the loss of native β-sheet structure is also revealed in DPP and DVE spectra. These experiments are related to projections of the complex 2D IR spectrum and show clear evidence of the two-peak structure expected for AP β sheets.

Our investigations are presented as follows. In the following section, we review the nonlinear spectroscopies used here and state the projection relationships that relate DVE and DPP spectra to the complex 2D IR correlation spectrum. The experimental methods for obtaining femtosecond 2D IR, DVE, and DPP spectra of proteins are given in the Experimental Section. The results and discussion are presented together in section IV. We first summarize the interpretation of protein 2D IR spectra with an emphasis on β-sheet structure and then present experimental probes of thermal denaturing using FTIR, 2D IR, DVE, and DPP and follow with an analysis of the temperature-dependent experiments using singular value decomposition. Conclusions are given in section V.

II. Nonlinear Infrared Experiments

The nonlinear experiments used here can be expressed in terms of the third-order nonlinear response function $\mathbf{R}^{(3)}(\tau_1, \tau_2, \tau_3)$ that describes the vibrational dynamics of a system subject to transition dipole interactions with three sequential electric fields.[31,63] The response function has information on molecular structure in the form of vibrational coordinates, couplings, dipole orientations, and the dynamics of the system that arises from interactions with its environment. For each experiment, a sequence of three femtosecond infrared fields, separated by sequential time delays τ_1 and τ_2, leads to a nonlinear polarization $\mathbf{P}^{(3)}(\mathbf{k_s}, \tau_1, \tau_2, \tau_3)$ that radiates a signal $\mathbf{E}_{sig}^{(3)}(\mathbf{k_s}, \tau_1, \tau_2, \tau_3)$ into a

wavevector matched direction $\mathbf{k_s}$ during the detection period τ_3. For dispersed vibrational echo experiments, the background-free signal is frequency-dispersed, and the power in each Fourier component of the radiated signal field is detected. In pump–probe experiments, two interactions are derived from a single pump pulse ($\tau_1 = 0$), and a third interaction with a time-delayed probe pulse leads to the radiation of a signal collinear with the transmitted probe. The transmitted probe is frequency-dispersed, and the pump-induced change in the probe intensity is characterized as a function of the detection frequency.

For 2D IR experiments, the radiated signal field during τ_3 is characterized through heterodyne detection for repeated measurements as a function of τ_1. A two-dimensional Fourier transform leads to a 2D IR spectrum in the conjugate variables (ω_1, ω_3) that respectively represent those vibrational transitions that were initially excited and then ultimately detected. The 2D IR correlation spectrum $\tilde{\mathbf{S}}_C$ is obtained from the sum of two complementary spectra, the rephasing and nonrephasing spectra $\tilde{\mathbf{S}}_C = \tilde{\mathbf{S}}_R + \tilde{\mathbf{S}}_{NR}$.[31,64] The rephasing and nonrephasing signals $\mathbf{E}_R^{(3)}$ and $\mathbf{E}_{NR}^{(3)}$ differ by their wavevectors $\mathbf{k}_R$ and $\mathbf{k}_{NR}$, respectively. For rephasing signals, the phase acquired by coherences during the evolution period, $e^{i\Omega\tau_1}$, is the conjugate of that for the detection period, $e^{-i\Omega\tau_3}$, whereas coherences in nonrephasing measurements evolve with the same phase during both τ_1 ($e^{-i\Omega\tau_1}$) and τ_3 ($e^{-i\Omega\tau_3}$). The 2D IR spectra of rephasing and nonrephasing signals have phase-twisted line shapes, elongated along the diagonal and antidiagonal directions, respectively, but the 2D IR correlation spectrum has proper absorptive 2D line shapes.[31,64] Nonetheless, the rephasing and nonrephasing spectra interpreted separately can reveal resonances hidden in the correlation spectrum or suppress unwanted spectral information.

Two-dimensional infrared experiments are perhaps the most complete characterization of the nonlinear response function that carries with it information on the molecular structure and dynamics of the system. They are therefore the most sensitive third-order probes for complex or congested spectra, such as the amide bands of proteins. As nonlinear probes, dispersed vibrational echo (DVE) and dispersed pump–probe (DPP) experiments should also be sensitive to much of the underlying structure and dynamics, without many of the technical challenges associated with the interferometric detection required for time-domain 2D IR experiments. DVE and DPP experiments reflect signals that arise from interactions with multiple vibrations and are projected onto one frequency axis.

The experimental characterization of the femtosecond nonlinear IR signal field is achieved by using a heterodyne detection scheme using a well-characterized local oscillator (LO) field $\mathbf{E_{LO}}$. For the 2D IR experiments presented here, we spectrally disperse the signal and LO fields in a monochromator, which effectively Fourier transforms the fields in the detection time period (τ_3) to its Fourier transform pair, ω_3. Ignoring any timing errors, the experimentally obtained 2D IR correlation spectrum can be written as

$$\tilde{\mathbf{S}}'_C(\omega_1, \tau_2, \omega_3) \propto \text{Re}\mathscr{F}[\mathbf{E_{LO}}(\omega_3)\, \mathbf{E}_R^{(3)}(\tau_1, \tau_2, \omega_3) +$$
$$\mathbf{E_{LO}}(\omega_3)\, \mathbf{E}_{NR}^{(3)}(\tau_1, \tau_2, \omega_3)] \quad (1)$$

where the Fourier transform is defined as

$$\mathscr{F}(Z) = \int_{-\infty}^{+\infty} Z e^{i\omega_1\tau_1}\, d\tau_1$$

The correlation spectrum represents the real part of the complex 2D IR spectrum

$$\tilde{\mathbf{S}}_C(\omega_1, \tau_2, \omega_3) = \tilde{\mathbf{S}}'_C(\omega_1, \tau_2, \omega_3) + i\, \tilde{\mathbf{S}}''_C(\omega_1, \tau_2, \omega_3) \quad (2)$$

In eq 1, the correlation spectrum is expressed in terms of the rephasing and nonrephasing signals, and the LO field is taken to be timed (in phase) with the third pulse. Note that each signal field contains both dichroic (in-phase) and birefringent (in-quadrature) contributions. For a resonant experiment, we assume that the dichroic contribution dominates.

The two-pulse DPP signal represents a heterodyne-detected nonlinear signal in which the transmitted probe field ($\mathbf{E_{pr}}$) acts as an intrinsic in-phase LO:

$$\tilde{\mathbf{S}}_{DPP}(\tau_1 = 0, \tau_2, \omega_3) \propto \text{Re}[\mathbf{E_{pr}}(\omega_3)\, \mathbf{E}_{PP}^{(3)}(\mathbf{k_{pr}}, \tau_1 = 0, \tau_2, \omega_3)] \quad (3)$$

Here the pump–probe signal field has both rephasing and nonrephasing contributions

$$\mathbf{E}_{PP}^{(3)}(\tau_1 = 0, \tau_2, \omega_3) =$$
$$\mathbf{E}_R^{(3)}(\tau_1 = 0, \tau_2, \omega_3) + \mathbf{E}_{NR}^{(3)}(\tau_1 = 0, \tau_2, \omega_3) \quad (4)$$

For a two-pulse DPP experiment, the first two interactions are with the same pump pulse and $\tau_1 = 0$. Using the projection-slice theorem, we can relate the DPP and DVE signals to projections of the 2D IR correlation spectrum along ω_1. It has been established that in the limit of weak sample absorbance the dispersed pump–probe measurements can be obtained from the 2D IR correlation spectrum by projecting it onto ω_3:[65]

$$\tilde{\mathbf{S}}_{DPP}(\tau_2, \omega_3) = \frac{\mathbf{E_{pr}}(\omega_3)}{\mathbf{E_{LO}}(\omega_3)} \int_{-\infty}^{\infty} \tilde{\mathbf{S}}'_C(\omega_1, \tau_2, \omega_3)\, d\omega_1 \quad (5)$$

The ratio of the $\mathbf{E_{pr}}$ and $\mathbf{E_{LO}}$ spectra in eq 5 would cancel only in the limit of weak absorption and matched dispersion in the sample and LO arms of the interferometer. Equation 5 forms the basis for phasing methods used to correct for timing uncertainties in our heterodyne-detected experiments.[65]

Similar relationships exist for the DVE measurement, a homodyne signal given as the square of the third-order nonlinear signal field. For the case presented here where $\tau_1 = 0$, the signal is a degenerate four-wave mixing signal in which all excitation pulses are timed to one another so that both rephasing and nonrephasing signals contribute

$$\tilde{\mathbf{S}}_{DVE}(\tau_1 = 0, \tau_2, \omega_3) \propto$$
$$|\mathbf{E}_R^{(3)}(\tau_1 = 0, \tau_2, \omega_3) + \mathbf{E}_{NR}^{(3)}(\tau_1 = 0, \tau_2, \omega_3)|^2 \quad (6)$$

Because the DVE is a homodyne measurement, the DVE spectrum can be related to the square of the absolute value of the projection of the complex 2D IR spectrum along ω_1

$$\tilde{\mathbf{S}}_{DVE}(\tau_1 = 0, \tau_2, \omega_3) \propto \frac{1}{I_{LO}(\omega_3)} \left| \int_{-\infty}^{\infty} \tilde{\mathbf{S}}_C(\omega_1, \tau_2, \omega_3)\, d\omega_1 \right|^2 \quad (7)$$

In this equation, the normalization by the intensity spectrum of the local oscillator corrects for the additional convolution with the local oscillator field used in measuring $\tilde{\mathbf{S}}_C$.

III. Experimental Section

The experimental methods for acquiring 2D IR experiments are summarized here but have been described in detail in ref 31. The experiments on the amide I band of RNase A are performed with 90-fs, mid-IR pulses centered at 6 μm. These

pulses have a bandwidth of $\sim$160 cm^{-1}, which is sufficient to excite the fundamental ($\nu = 0 \rightarrow 1$) and the anharmonically shifted $\nu = 1 \rightarrow 2$ transitions of interest. Three time-coincident $\sim$150-nJ pulses, E$_\alpha$, E$_\beta$, and E$_\chi$, are crossed in a box geometry and focused to a 100-μm diameter at the sample. The polarization and intensity of each of the beams were controlled using ZnSe wire grid polarizers and MgF$_2$ half-wave plates. The relative timings between the three pulses are controlled using retroreflectors mounted on motorized linear stages (Aerotech, ANT-50L) with a resolution of 10 nm (0.067 fs), an accuracy of 300 nm (2 fs), and a repeatability of 50 nm (0.33 fs). The nonlinear signal field is generated in the phase-matched direction $\mathbf{k_s} = -\mathbf{k_\alpha} + \mathbf{k_\beta} + \mathbf{k_\chi}$. The signal is isolated after the sample and overlapped spatially and temporally with a fourth pulse, a local oscillator field. Heterodyne detection is performed by dispersing the two beams in a 190-mm monochromator with a 40 lines/mm grating. The dispersed signal is collected at the focal plane with a liquid-nitrogen-cooled 64-pixel MCT array detector. Two-dimensional IR data were taken in the crossed (*ZZYY*) polarization geometry. Rephasing ($\mathbf{k_s} = -\mathbf{k_1} + \mathbf{k_2} + \mathbf{k_3} \equiv \mathbf{k_R}$) and nonrephasing ($\mathbf{k_s} = \mathbf{k_1} - \mathbf{k_2} + \mathbf{k_3} \equiv \mathbf{k_{NR}}$) experiments are performed for $\tau_2 = 0$ by altering the time sequence of the $\mathbf{k_\alpha}$ and $\mathbf{k_\beta}$ pulses.

Arrays of dispersed heterodyned signals with a spectral resolution of $\sim$4 cm^{-1} in the ω_3 dimension are collected as a function of τ_1 in 4-fs steps for both rephasing and nonrephasing configurations. The data are collected for τ_1 delays ranging from -0.06 to 2 ps and from -0.06 to 1 ps for the rephasing and nonrephasing experiments, respectively. A Fourier transform along the τ_1 axis yields the individual 2D rephasing and nonrephasing spectra, and the sum of these gives the 2D IR correlation spectrum. The resolution in the ω_1 dimension after Fourier transformation is 0.5 cm^{-1}. Dispersed pump–probe spectra were obtained using a fifth pulse, a tracer beam that follows the path of the signal, as the probe and E$_\chi$ as the pump at $\tau_2 = 0$ to help us phase the 2D IR spectra.

The treatment of the raw data to yield properly "phased" 2D IR correlation spectra that correct for timing or phase errors has been described before,[31] but we use a slightly different method for the data presented here. The first step of the phasing procedure involves using the dispersed pump–probe trace at $\tau_2 = 0$ to find the error in the τ_1 timing ($\Delta\tau_1$) for the rephasing and nonrephasing signals collected as a function of ω_3 and τ_1. We make use of the fact that the slices corresponding to $\tau_1 = 0$ of the rephasing and nonrephasing data matrices are each equal to the dispersed pump–probe array at $\tau_2 = 0$ and identical to each other.[65] This allows us to correct for the finite values of $\Delta\tau_1$ for the individual rephasing and nonrephasing signals. To ensure that we have phased the data correctly, we transform the individual signals along τ_1 and sum their real parts to obtain an absorptive 2D IR correlation spectrum, $\tilde{S}'_C$. The projection of $\tilde{S}'_C$ along ω_1 is compared to the dispersed pump–probe data. Any differences are compensated by multiplying the complex value rephasing and nonrephasing 2D spectra individually with the phase factor exp($i\omega_3\Delta\tau_3 + \phi$). Note that the value of $\Delta\tau_3$, which accounts for our inability to time the signal and LO fields exactly, can be different for the rephasing and nonrephasing signals. The variable ϕ accounts for phase errors arising from the imbalances in the interferometer. After multiplying the complex rephasing and nonrephasing 2D spectra as described above, we again sum their real parts and compare the projection of $\tilde{S}'_C$ along ω_1 to the dispersed pump–probe data. This process is iterated until an optimal match between the projection of $\tilde{S}'_C$ along ω_1 and the dispersed pump–probe data is obtained.

Dispersed pump–probe spectra were obtained in the crossed-polarization geometry using the tracer beam as the probe and E$_\chi$ as the pump and setting $\tau_2 = 0$. By chopping the pump beam, the differential probe transmission through the sample is observed on the array detector. The DVE measurements reflect background-free four-wave mixing signals generated with time-coincident pulses ($\tau_1 = \tau_2 = 0$). The spectra were obtained in the all-parallel (*ZZZZ*) polarization geometry by dispersing the signal in the monochromator and measuring the integrated power at a given frequency component with the array detector. FTIR spectra were collected on a Mattson Infinity Gold FTIR spectrometer with a frequency resolution of 2 cm^{-1}. For all measurements, the sample was placed in a homebuilt, temperature-controlled cell consisting of two 1-mm-thick CaF$_2$ windows separated by a 50-μm-thick Teflon spacer. The temperature of the cell was regulated by circulating water from a bath that is temperature-controlled to within 0.1 °C. The temperatures quoted for the protein solution are those measured by a thermocouple mounted on the CaF$_2$ window.

The RNase A sample was purchased from Sigma Aldrich (R5500). It was dissolved in a 20 mM D$_2$O phosphate buffer solution of pH* 7 (uncorrected pH) for a final concentration of 16.5 mg/mL. All of the samples were incubated at 60 °C for 1 h prior to performing the experiments to allow for H/D exchange. This solution allowed for reversible thermal denaturing and folding of the protein when tested by FTIR, following a temperature cycle up to 80 °C. The sample had a peak OD of 0.2 for the 2D IR and DPP experiments and 0.5 for the DVE experiments.

IV. Results and Discussion

A. 2D IR Spectroscopy of Proteins with Antiparallel β Sheets. We begin by discussing the linear and 2D IR spectroscopy of amide I transitions of AP β sheets. Empirical relationships have existed for some time linking AP β-sheet structure in proteins with a pair of resonances in the amide I spectral region: a strong one that lies between 1610 and 1640 cm^{-1} and a weak one between 1680 and 1700 cm^{-1}.[22,41,49] Although these modes can be clearly distinguished in β-sheet aggregates or proteins with high AP β-sheet content, they are more difficult to see in proteins where different secondary structural elements are present or where there is considerable conformational disorder within the β-sheet regions of the proteins.

We have found that the two amide I features are revealed in 2D IR spectra of antiparallel β-sheet-containing proteins through the formation of a cross peak between the low- and high-frequency transitions.[47,48] The clearest example is the 2D IR correlation spectrum of poly-L-lysine at high pH, a model system for studying AP β-sheet structure, which shows cross peaks between the two amide I resonances at 1611 and 1680 cm^{-1} (Figure 1b).[48] The 2D IR spectrum shows two diagonal and two cross peaks, each composed of doublets of opposite sign. This is the spectrum expected for two vibrational eigenstates that arise from coupled anharmonic vibrations.[31] As originally described by Miyazawa,[49] these two observed amide I transitions can be understood in terms of the structure and vibrational couplings for an idealized AP β sheet.[47] The dominant transitions can be predicted from the symmetry of the four-oscillator unit cell pictured in Figure 1. The IR oscillator strength is carried by two vibrational modes (a+ and a−) involving antisymmetric stretching (a) of the 1−4 and 2−3 dimer pairs, with in-phase (+) and out-of-phase (−) vibrations between the 1 and 2 oscillators. The more intense, lower-frequency transition corresponds to the a− vibration, whereas the weaker, high-frequency transition arises from the a+ vibration.
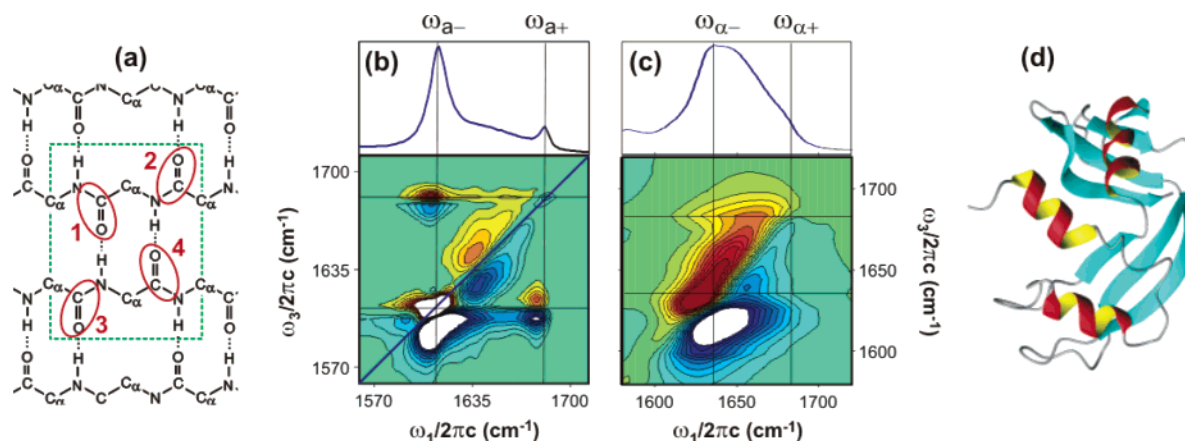
Figure 1. (a) Schematic showing the unit cell for an idealized antiparallel β sheet, identifying four amide I oscillators (primarily CO stretch with CN stretching and other contributions). For the idealized structure, there are four vibrational states that involve the symmetric (s) and asymmetric (a) stretching of the 1−4 and 2−3 dimer pairs. The IR oscillator strength is carried by the a+ and a− modes involving in-phase (+) and out-of-phase (−) vibrations between the 1 and 2 oscillators.[47] The s states are only weakly IR allowed. (b) Linear FTIR and 2D IR correlation spectra of poly-L-lysine at pH* 11.4 in the amide I region. Nineteen equally spaced contours are plotted between −20 and 20% of the peak maximum. The resonance frequencies of the two dominant IR-active transitions of an extended pleated antiparallel β sheet are labeled. (c) Linear and 2D IR amide I correlation spectra of RNase A at 25 °C in the crossed-polarization geometry. Twenty-one equally spaced contours are drawn from −60 to 60% of the maximum amplitude in the 2D spectrum. (d) Ribbon diagram of the crystal structure of RNase A (7RSA).[50]

The 2D IR spectra of proteins with AP β sheets also show this structure, although it appears different.[48] The position and shape of the spectral features are sensitive measures of the vibrational couplings within the sheet, the size and geometry of the sheet, and structural or energetic disorder associated with the peptide units within the sheet.[47,48] The vibrations of finite or disordered sheets may lead to overlapping transitions of slightly varying symmetry from the a− and a+ designations used for the idealized sheet, and for that reason we label the resonances α− and α+ in proteins. The frequency of the low-frequency α− transition is sensitive to the size and geometry of the β sheet, leading to considerable inhomogeneous broadening in proteins with conformational disorder. This is observed as the stretching of the α− diagonal and cross peaks. However, the α+ transition is insensitive to disorder.

These effects are apparent in the 25 °C 2D IR correlation spectrum of RNase A shown in Figure 1c. The clear eight-peak structure seen in polylysine is not observed. One of the cross peaks between the two vibrations of the AP β sheets is seen as a ridge along $\omega_3 = 1684$ cm^{-1}. This arises from a distribution of α− frequencies and a correspondingly narrow distribution of α+ frequencies, expected for a protein with β-sheet structures of varying length, strand number, and conformation (Figure 1d). The presence of the other ($\omega_1 > \omega_3$) cross peaks is indicated by the decrease in intensity of the negative band elongated along the diagonal axis and constructive interferences that stretch the negative feature along $\omega_3 \approx 1620$ cm^{-1}. The spectral resonances along the diagonal, associated with the α-helices, turns, and random coils, are diagonally elongated, indicative of strong inhomogeneous broadening. The net effect, now observed in several β and α/β proteins, is that interference effects between the negative and positive lobes of the diagonal and cross peaks arising from a narrow α+ transition and a broadened α− transition, combined with diagonally elongated resonances from additional amide transitions, leads to a characteristic Z-shaped contour profile for the amide I region in the 2D IR spectrum.[48]

Despite suffering from spectral congestion, it is clear to see that the 2D IR correlation spectrum provides considerable additional information compared to the FTIR spectrum by accessing a second frequency dimension. Two-dimensional IR spectra reveal the underlying two-peak structure associated with
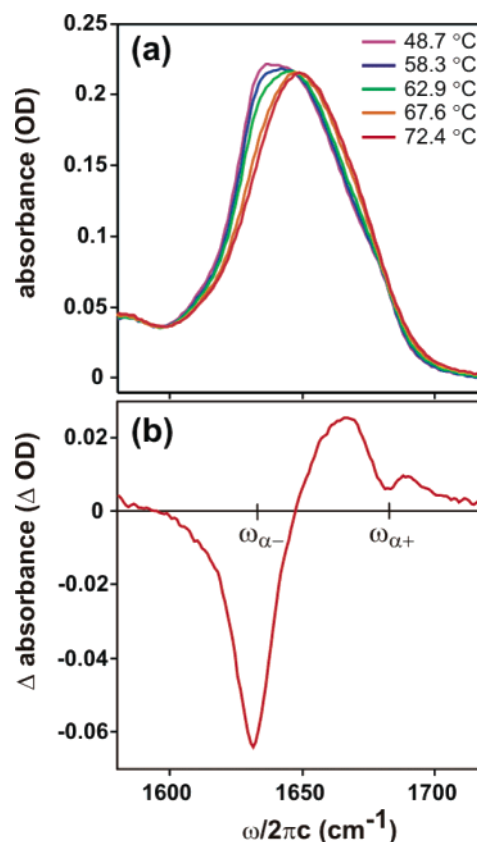
Figure 2. (a) Temperature-dependent amide I FTIR spectra of the thermal denaturing of RNase A with temperatures color coded. (b) Difference between 72.4 and 48.7 °C FTIR spectra with the frequencies of the characteristic β-sheet transitions labeled.

the antiparallel β sheets and separate these from other components such as diagonal resonances near 1645−1650 cm^{-1} that presumably arise from the α-helices and/or disordered regions.

B. FTIR Spectra. Figure 2 shows the temperature-dependent FTIR spectra of RNase A at pH* 7 in the range of 49−72 °C. The spectrum at 49 °C is asymmetric with a broad maximum in the region of 1636 cm^{-1} and a weak shoulder at 1680 cm^{-1}.

Both of these regions correspond to the main amide I transitions of the AP β-sheet structure. As the temperature increases, the overall shape of the spectrum becomes more symmetric, and the spectrum shifts to higher frequencies so that the main peak is centered at 1649 cm^{-1} at 72 °C. The net absorbance change between high and low temperatures, seen in Figure 2b, shows that there is a loss of intensity at two transition frequencies that correspond closely to those expected for the $\alpha+$ and $\alpha-$ modes. The overall changes are consistent with the loss of two transitions, a 26-cm^{-1}-wide band at $\omega_{\alpha-} = 1632$ cm^{-1} and a 10-cm^{-1} band centered at $\omega_{\alpha+} = 1682$ cm^{-1}, together with an increase of a 74-cm^{-1}-wide Gaussian spectral component centered at 1649 cm^{-1}. If we correlate these observations to changes in the secondary structural elements of RNase A using empirical relations, this change reflects a depletion of the β-sheet structure and an increase in the α-helical, turns, and/or random coil structures. The $\alpha+$ transition is insensitive to the disorder of the β sheet, and a comparison of its 10-cm^{-1} line width with the 26-cm^{-1} width of the structure-sensitive $\alpha-$ transition forms a measure of the structural inhomogeneity of the native β sheet. The maximum change observed in the FTIR difference spectra ($\Delta T = 25$ °C) corresponds to ~30% of the maximum absorbance in the amide I resonance at 50 °C. Further analysis of the spectra using the singular value decomposition method is given in section IVE.

C. Two-Dimensional IR Spectra. Figure 3 shows the temperature-dependent 2D IR spectra of RNase A between 58 and 72 °C, the temperature range over which the largest changes are observed in the FTIR spectra. Only small changes are observed between the native state at 25 °C (Figure 1) and the 58 °C spectrum. Spectra in this range show the signatures of AP β-sheet structure through the stretching of cross peaks and constructive interference along ω_1, leading to the Z-shaped contour profile discussed earlier. As the temperature increases above 58 °C, the dominant peak on the diagonal axis ($\omega_1 = \omega_3$) shifts its maximum to higher frequency, its antidiagonal width increases, the Z-shaped contour profile disappears, and the overall spectral shape becomes more symmetric. The disappearance of the Z indicates a loss of the stretched cross peak between the $\alpha+$ and $\alpha-$ transitions of the AP β-sheet structures as the protein denatures. This is consistent with disrupting the amide I vibrational couplings due to the melting of β sheets. The disappearance of the cross peak is also seen in the slices of the 2D IR spectra taken along $\omega_1 = 1636$ cm^{-1} and plotted adjacent to each spectrum. At 72 °C, there is no distinct cross peak seen along ω_3 for $\omega_1 = 1636$ cm^{-1}. Instead, the 72 °C spectrum appears as a symmetric doublet of diagonally elongated resonances characteristic of a classic inhomogeneously broadened transition that is characteristic of a highly disordered system. The small residual elongation observed for $\omega_3 = \omega_{\alpha+}$ and $\omega_{\alpha-}$ indicates that the denatured state is not completely random and that residual AP hydrogen bonding configurations between amide oscillators on adjacent strands are still present in this denatured state. This should be expected because four disulfide bridges stabilize the β sheets in RNase A.

Perhaps the clearest evidence for the melting of β-sheet structure is observed in the difference of 2D IR correlation spectra at 25 and 72 °C, as shown in Figure 4. This spectrum highlights the disappearance of the eight-peak structure expected for the $\alpha+$ and $\alpha-$ transitions of AP β sheets, in addition to the shift of spectral intensity to the blue on thermal denaturing. The difference spectrum also gives an indication of the shape of the elongated $\alpha+/\alpha-$ cross peaks in the native state. The spectrum indicates that 2D IR spectroscopy is sensitive to AP
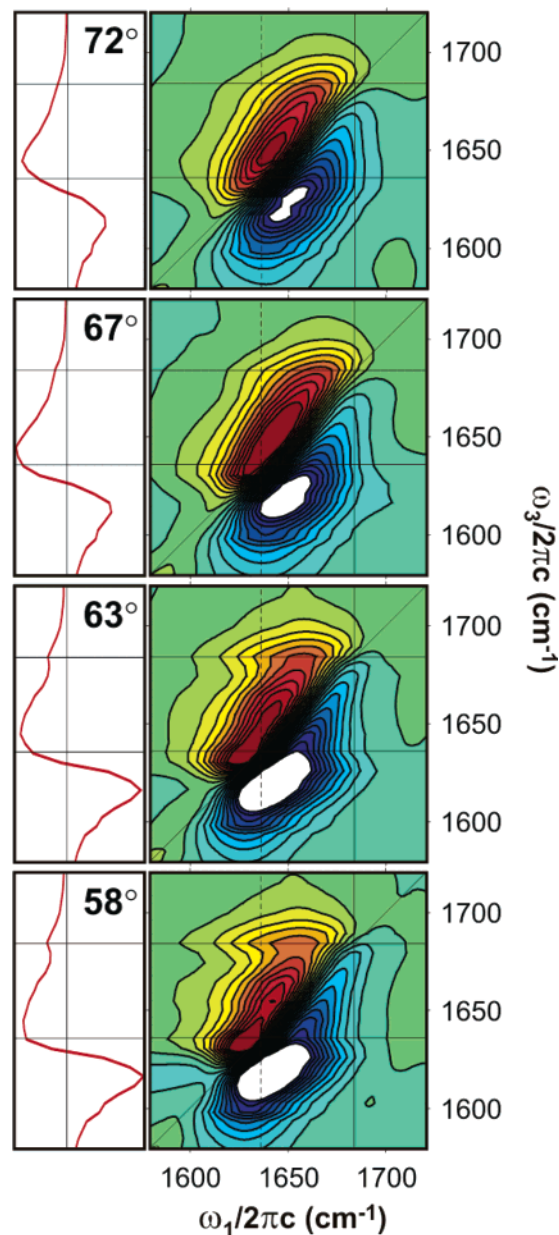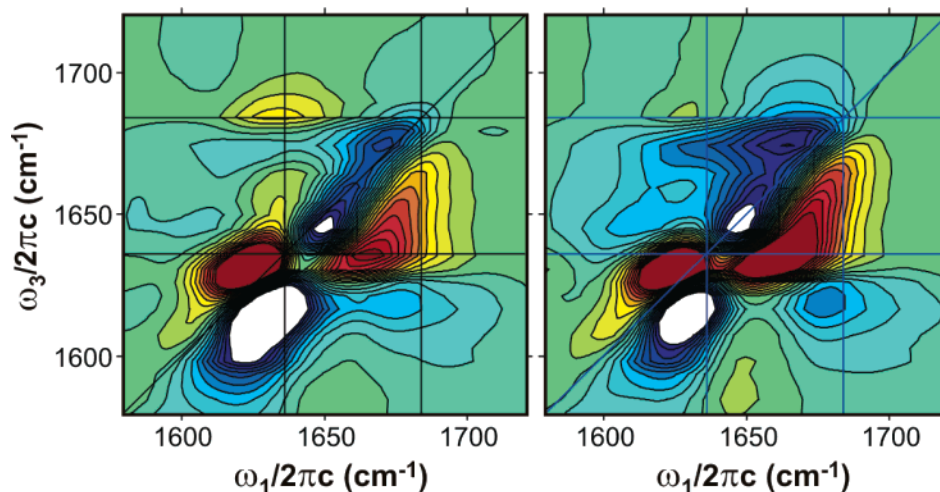

Figure 3. Temperature-dependent 2D IR correlation spectra $\tilde{S}'_C$ of RNase A obtained in the crossed-polarization geometry. Temperatures from top to bottom are 72.2, 67.4, 62.7, and 57.9 °C. The left panel of each 2D IR spectrum displays the slice along ω_3 corresponding to $\omega_1 = 1636$ cm^{-1} (solid line). All 2D IR spectra have been normalized to the maximum positive amplitude of the 25 °C spectrum. Twenty-one equally spaced contours are drawn from −60 to 60% of the maximum amplitude for all of the 2D IR correlation spectra. The largest changes in the 2D IR spectra are observed between 63 and 72 °C.

β-sheet structures in proteins and that the $\alpha+/\alpha-$ features of β sheets are still clearly present in α/β globular proteins such as RNase A.

Further evidence for the presence of a cross peak in the native state and its disappearance on thermal denaturing is seen in the absolute value nonrephasing (NR) spectra. Two-dimensional IR NR spectra at 25 and 72 °C, which show similar effects to the correlation spectra, are shown in Figure 5. The additive phase relationship in τ_1 and τ_3 allows nonrephasing spectra to suppress inhomogeneous line shapes along the diagonal axis.[31] The NR spectrum at 25 °C reveals the stretched shape of the $\alpha+/\alpha-$ cross peak expected for β sheets with intrinsic disorder in the native state due to variation in the number of strands in the

Figure 4. (Left) Two-dimensional IR difference spectrum, $\Delta\tilde{S}'_C = \tilde{S}'_C$ (25 °C) − $\tilde{S}'_C$ (72 °C). (Right) Second component $\sigma^{(2)}$ of the singular-value decomposition of temperature-dependent 2D IR correlation spectra. Each spectrum has been normalized to its maximum intensity, and 21 equally spaced contours are plotted from −40 to 40%.
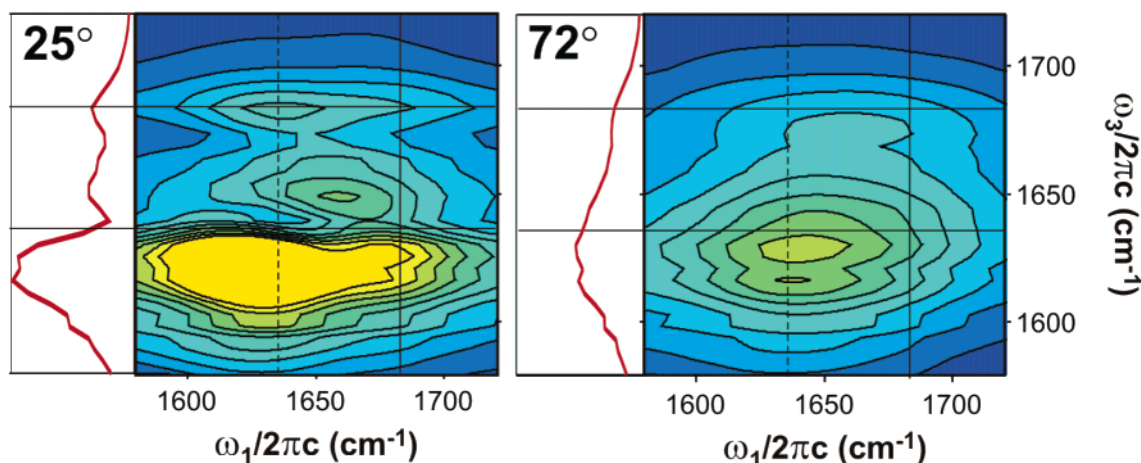

Figure 5. Absolute value nonrephasing spectra $|\tilde{S}_{NR}|$ of RNase A for the native and thermally denatured states obtained in the crossed-polarization geometry. The left panel of each spectrum displays the slice along $\omega_1 = 1636$ cm^{-1}. The 72 °C spectrum has been normalized to the maximum positive amplitude of the spectrum at 25 °C. Eleven equally spaced contours are drawn from 0 to 60% of the maximum amplitude of the 25 °C spectrum.

sheet, the variation in hydrogen bonding geometry in the sheet, and the deviation of the sheet from planarity.[48] Because of its insensitivity to inhomogeneous broadening, there is considerably less amplitude along the diagonal in the 2D IR NR spectrum between 1640 and 1670 cm^{-1}. Transitions in this region are commonly associated with random coils, turns, and α-helices. Random coils would likely be suppressed in the NR spectrum, but the distinct peak observed at (1660, 1650) cm^{-1} could very likely arise from the α-helices in RNase A. The *A* mode for the amide I vibrations of the helices would be expected to carry most of the oscillator strength. As the protein is denatured by raising the temperature to 72 °C, we note a loss of the stretched cross peaks (particularly for $\omega_1 < \omega_3$), a loss of the diagonal feature at 1650 cm^{-1}, an overall blue shift in the peak signal, and a more symmetric line shape. Additionally, the integrated amplitude of the spectrum decreases greatly, also reflecting a much more inhomogeneous system at high temperature. These observations are all consistent with the disruption of the vibrational couplings due to the melting of β sheets and a more random thermally denatured state.

D. Dispersed Nonlinear Signals: Pump−Probe and Vibrational Echoes. Although 2D IR spectra are perhaps the most

revealing infrared probes of protein vibrations, they are technically demanding and time-consuming to acquire in comparison to other nonlinear experiments. Thus, as alternate probes, dispersed pump−probe and vibrational echo signals are appealing, particularly for application to transient studies of protein folding. In addition to being easier to acquire, they can be interpreted in terms of projections of 2D data onto the ω_3 axis. As discussed above, for the DPP measurement this is a projection of the real part of the complex correlation spectrum and, in the case of the DVE, the absolute square value of the projection of the complex correlation spectrum. In either case, the combination of multiple negative and positive features in the 2D IR spectrum makes it clear that these projections cannot be interpreted simply and will usually involve the interference between various signal contributions. Nonetheless, for either experiment, the 2D IR correlation spectra of RNase A in Figure 3 suggest that the two-peak $\alpha+/\alpha-$ structure indicative of β sheets should be revealed.

Figure 6 shows the temperature-dependent DPP and DVE spectra obtained at $\tau_2 = 0$ and $\tau_1 = \tau_2 = 0$, respectively. At low temperatures, the DPP spectra show signatures of three features, which can be assigned in terms of a projection of the

Conformational Change during Thermal Unfolding

J. Phys. Chem. B, Vol. 108, No. 39, 2004 **15339**
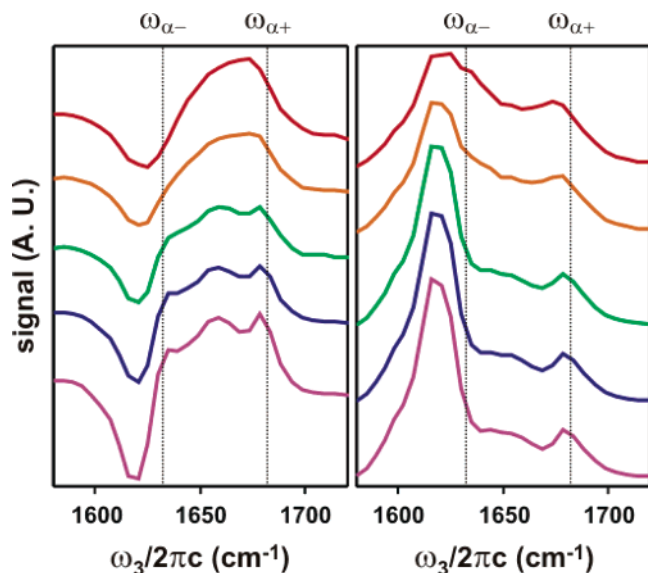
Figure 6. Temperature-dependent dispersed pump−probe (left) and dispersed vibrational echo (right) spectra obtained at $\tau_2 = 0$ and $\tau_1 = \tau_2 = 0$, respectively. The temperatures of the traces increase from bottom to top corresponding to 48.2, 57.9, 62.7, 67.4, and 72.2 °C.

2D IR correlation spectrum. Two sharper features below $\omega_{\alpha+}$ and $\omega_{\alpha-}$ arise from projections of the oppositely signed ridges of the Z pattern, and an additional resonance from the diagonal feature is observed at 1660 cm^{-1}. As the temperature increases, the three-peak structure in the positive lobe starts to disappear, the overall amplitude decreases, and the positive and negative line shapes look symmetric. This directly corresponds to the spectral changes in the 2D IR correlation spectra where the Z-shaped contour profile disappears at high temperatures, leaving two almost-symmetric and oppositely signed peaks along the diagonal.

The DVE spectra show similar dramatic changes. At the lowest temperature, we see a two-peak structure with peaks at 1618 and 1684 cm^{-1} that looks remarkably similar to the FTIR spectrum of poly-L-lysine at high pH. Because of interference effects, it is not straightforward to relate a projection of the 2D IR spectrum to the DVE signal. Nonetheless, one can see that the peak at 1684 cm^{-1} corresponds to the high-frequency amide I mode of the AP β sheet, whereas the low-frequency peak results from the interference of the positive and negative features in the 2D IR spectra. This peak can be thought of as arising from the projection of the base of the Z onto the ω_3 axis. The nonlinear scaling of the transition dipole moment in the DVE spectra results in far greater temperature-dependent changes as opposed to those in the linear FTIR spectra. As the temperature increases, we see that the relative ratio of the low- and high-frequency features in the DVE spectra drops, the low-frequency peak moves to ∼1630 cm^{-1}, the high-frequency peak moves to ∼1679 cm^{-1}, and the spectral amplitude in the central region around 1650 cm^{-1} increases.

Although, the spectra displayed in Figure 6 involve only one frequency axis, their origin in a nonlinear experiment leads to features that are more sensitive to the changes in the amide I region accompanying the thermal denaturation of RNase A than the traditional linear FTIR spectra shown in Figure 2. Any third-order nonlinear IR experiment on multiple coupled vibrations will have a signal that arises from transitions to multiple singly and doubly excited vibrational states and will thereby be sensitive to vibrational couplings. Even with the projections involved, the DPP and the DVE spectra can be related to the

more intuitive 2D IR spectra that encode the vibrational couplings between peptide vibrations making them a more sensitive probe of underlying protein structure than traditional FTIR.

E. SVD Analysis of Spectral Changes. The amide I band in FTIR spectroscopy has been used to follow the denaturation of proteins due to temperature, pressure, and chemical denaturants. Oftentimes, the changes in the FTIR spectrum are too minute and difficult to correlate to structural changes. This has led to various spectral decomposition techniques to try to glean structural information, in particular, the amount of secondary structure in the denatured state versus that in the native state.[66] In a similar manner, we have applied a singular-value decomposition analysis to interpret the temperature-dependent spectral changes observed in the linear and nonlinear infrared probes of RNase A denaturing.

Singular-value decomposition (SVD) can be used to analyze the common spectral components of a temperature-dependent or other series of linear and nonlinear spectra using techniques for the diagonalization of rectangular matrices.[67−69] The temperature-dependent spectral data matrix is built by arranging temperature components in columns and spectral components in rows. Two-dimensional IR data matrices are converted to a one-dimensional array by appending rows one after another. Then, the spectrum at temperature T can be expressed as a linear combination of a series of SVD component spectra

$$\mathbf{S}(T) = \sum_{i=1}^{n} c_i(T)\,\boldsymbol{\sigma}_i \qquad (8)$$

The coefficients c_i form the temperature-dependent amplitudes of a series of common spectral components σ_i for the series of temperature-dependent spectra. The first component c_1 reflects the mean spectral amplitudes for all temperatures, whereas the second spectral component c_2 reflects the difference in spectral amplitude between temperatures. Higher components reflect increasingly subtle variations in the spectral features between temperatures. Because the second component coefficient c_2 is the most sensitive to the spectral change, it is an effective parameter for constructing melting curves for the thermal unfolding of proteins. For the case of two-state folding, the temperature variation of c_2 can be used to analyze the folding thermodynamics.

The second spectral components σ_2 obtained from the SVD of the temperature-dependent FTIR, DVE, and DPP spectra are shown in Figure 7 together with the difference spectra between the high- and low-temperature spectra. In each case, the σ_2 are similar to the difference spectra and show features that clearly reflect the concerted loss of $\alpha+$ and $\alpha-$ transitions on increasing the temperature. In the case of the FTIR and the DVE, there is also an increase of amplitude in the 1650−1660-cm^{-1} range. These observations are consistent with the loss of β-sheet structure and the increase of the random component. We find that the amplitudes of the third SVD component for FTIR and DVE are very small, 0.7 and 1.5% relative to σ_1, whereas for the DPP, the amplitudes of σ_2 and σ_3 are comparable, 15 and 12%, respectively.

The second SVD component σ_2 of the temperature-dependent 2D IR spectra is shown in Figure 4 together with the difference in the 2D IR spectrum at 25 and 72 °C. The two spectra are very similar, both showing the disappearance of the eight-peak structure expected for diagonal and cross peaks of $\alpha+$ and $\alpha-$ transitions of antiparallel β sheets. The SVD analysis indicates that in large part the dominant spectral changes observed through
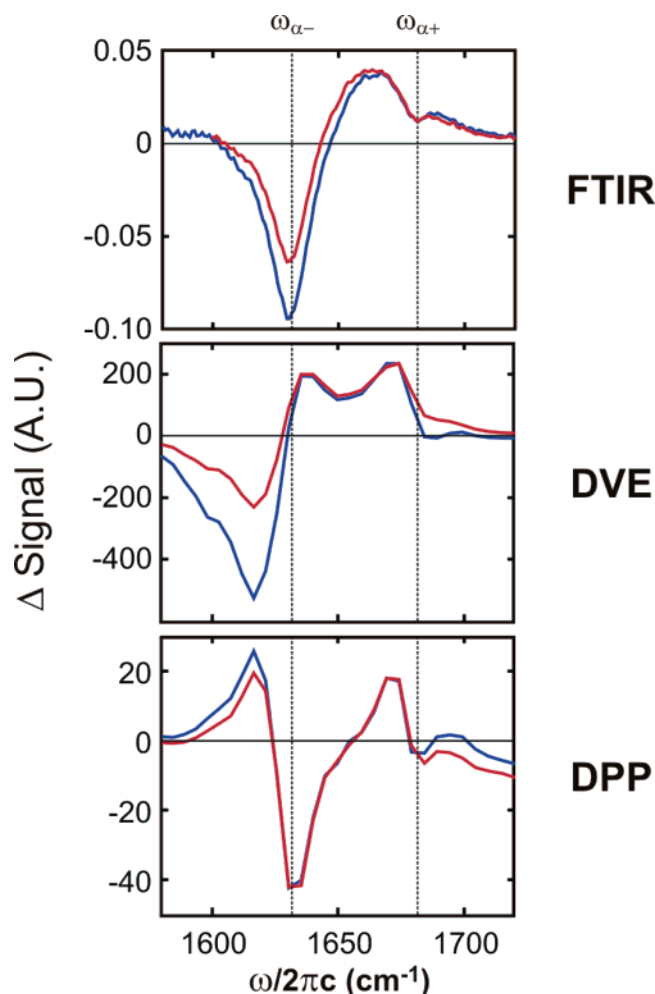
Figure 7. Difference spectra between the highest- and lowest-temperature $S(T_n) - S(T_1)$ (blue) and the second SVD component spectra σ_2 (red) of FTIR, DVE, and DPP.

2D IR over the entire temperature range are consistent with the disappearance of β-sheet structure. More so than the difference spectrum, the SVD analysis also emphasizes the growth of an extra diagonal feature in the $\sim$1650-cm^{-1} region. Both spectra are similar to the poly-L-lysine spectrum except for the absence of the $\alpha+$ mode in the diagonal slice ($\sim$1684 cm^{-1}) because of its small dipole strength. The existence of the strong, broad diagonal peaks between $\alpha+$ and $\alpha-$ reflects the increase of the random structure portion at higher temperature. Note that cross peaks are clearly shown in the off-diagonal regions. Those in the lower right region ($\omega_1 > \omega_3$) are stronger than those in the upper left region ($\omega_3 > \omega_1$) because of the constructive and destructive interference with the wings of the strong $\alpha-$ mode peaks.

The melting curves derived from the temperature-dependent amplitude of the second SVD component c_2 are shown in Figure 8. Although the shapes of the melting curves vary somewhat between experiments, all show that the protein denaturation occurs at approximately 65 °C. The melting temperatures (midpoint) obtained from FTIR and DVE are 66 and 65 °C, respectively. The SVD analysis of the four experiments indicates that the 65 °C transition, common to all experiments, is associated with the melting of β-sheet structure. Although the DPP and 2D IR spectra are not sampled at as many temperatures as the FTIR and DVE, it is clear that there are differences in the melting curves for temperatures <60 °C. Note that the

melting curve of DVE deviates from the single sigmoid shape and shows evidence of a pretransition at 43 °C. A similar curve is obtained from FTIR. The existence of a pretransition has been observed by FTIR, CD, and Raman spectroscopy and is attributed to the partial unfolding of helix II with modification of the β strand 43−49.[52,54]

In the case of two-state folding kinetics, the temperature-dependent series should be well described by only the first and second SVD components, reflecting continuous amplitude changes between the spectra of reactants and products. For this limit, when $c_1(T)$ remains constant and c_i components for $i > 2$ are negligible, the normalized second SVD component follows the fractional change of one of the two equilibrium components. Then, c_2 can be used in a thermodynamic analysis, as discussed in the Appendix. This is only the case when the signal amplitude scales linearly with the sample concentration, which is the case for FTIR, 2D IR, and DPP experiments. For background-free DVE experiments, this analysis is not generally applicable but possible when the changes are small compared to the average spectrum and can be linearly expanded (Appendix). In the case of RNase A, the melting curves in Figure 8 indicate that the folding is not two-state when characterized over the entire temperature range. If we limit our analysis to temperatures above 50 °C, then the FTIR and DVE results are described by the first and second components, and the average values of the enthalpy and entropy of denaturation obtained are $\Delta H = 103$ kcal/mol and $\Delta S = 306$ cal/mol·K for the DVE and $\Delta H = 82$ kcal/mol and $\Delta S = 240$ cal/mol·K for the FTIR, consistent with previous results.[52,70,71]

V. Conclusions

The thermal denaturing of AP β-sheet secondary structure in RNase A has been investigated using a number of nonlinear infrared probes of the amide I transitions. Each of these experiments is sensitive to changes in protein secondary structure on thermal denaturing. Two-dimensional IR spectroscopy offers the most information about protein conformation and is particularly sensitive to AP β-sheet structure through the cross peaks between the $\alpha-$ and $\alpha+$ transitions. These cross peaks persist even for distorted β sheets in α/β proteins such as RNase A. The distinct eight-peak structure in the 2D IR difference spectrum of native and denatured states indicates that the vibrational couplings between amide I oscillators in AP β-sheet interstrand registry disappear. This is consistent with the melting of the β sheet in the thermal denaturing process, although the highest-temperature spectrum indicates some residual AP β-sheet configurations. With ongoing improvements in models for amide I couplings, quantitative modeling of these 2D IR spectra is becoming possible, which should allow them to reveal the specifics of how the protein structure unfolds through the alteration of regions of vibrational couplings. Strategies have been discussed for describing the unfolding or conformational heterogeneity of small peptides from 2D IR spectra,[72,73] and similar methods could be brought to bear on proteins.

The DVE and DPP spectra also show clear features associated with the β sheets. These experiments are simpler to perform than 2D IR measurements and reveal more underlying features in the amide I region than conventional FTIR. As a result, the thermal denaturing of β sheets is observed more clearly in these two methods compared to FTIR, even though both are presented as a spectrum in one frequency axis. The DVE and DPP experiments are related to the complex 2D IR correlation spectrum through projection relationships. Nonetheless, the interpretation of these signals is not trivial as a result of

Conformational Change during Thermal Unfolding

J. Phys. Chem. B, Vol. 108, No. 39, 2004 **15341**
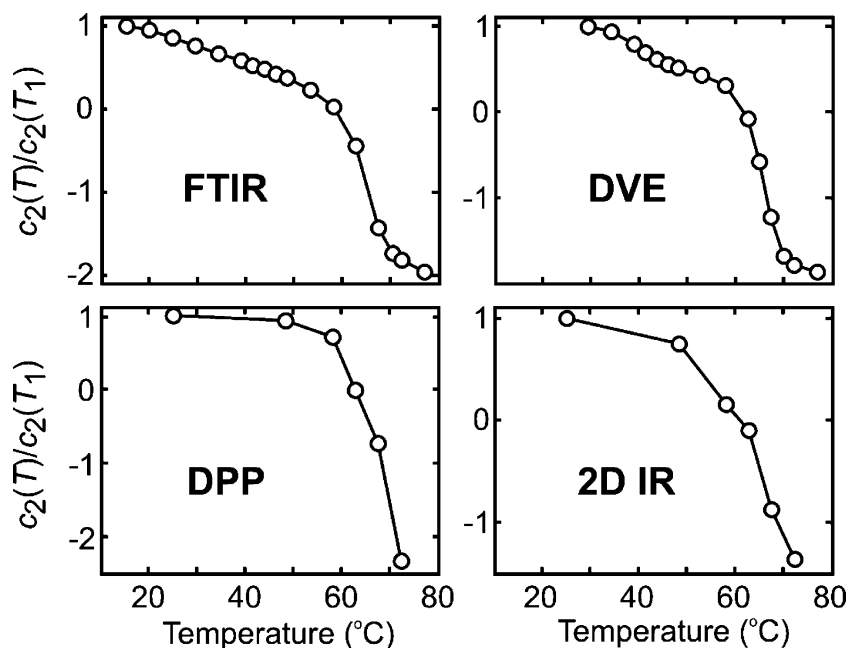
Figure 8. Thermal melting curves obtained from the scaled second components $c_2(T)/c_2(T_1)$ of the FTIR, DVE, DPP, and 2D IR spectra. $c_2(T_1)$ is the coefficient of the spectrum at the lowest temperature T_1.

interference effects between negative and positive features in projections of the 2D IR spectrum and nonlinear scaling of the signal in population. Melting curves for RNase A denaturing were obtained from an SVD analysis of the nonlinear spectra. These reveal a pretransition at 43 °C followed by the main denaturing of the β structure of RNase A at 65 °C.

The high time resolution and conformational sensitivity of nonlinear infrared experiments on proteins make them appealing as direct time-resolved probes of protein conformational changes. These methods can be applied to transient changes following a rapid initiation event. Two-dimensional IR experiments can be used as probes of conformational change following an optical initiation such as isomerization,[13] pH jump, or photorelease. The relative simplicity and background-free detection of DVE experiments make them promising probes of folding or unfolding following a temperature jump because they will not be as susceptible to heating-induced artifacts as the interferometrically detected 2D IR experiment. Such experiments should allow structurally sensitive studies of protein folding or binding processes on the important nanosecond to millisecond time scales. The structural information available is not atomistic but is obtained through a characterization of delocalized vibrational states that reflect protein conformation. Such a probe is particularly valuable for probing mesoscopic conformational changes and is thus of significance for describing protein folding coordinates and free-energy landscapes.

Appendix: Thermodynamics of Two-State Folding from SVD Analysis

Consider the case that the spectrum $\mathbf{S}(T_i)$ at all temperatures T_i can be expressed with the first and second SVD components σ_1 and σ_2,

$$\mathbf{S}(T_i) = c_1(T_i)\, \sigma_1 + c_2(T_i)\, \sigma_2 \qquad (A1)$$

If the spectral amplitude depends linearly on concentration, then in the case of two-state folding the spectrum can also be expressed by the linear combination of the spectra of lowest temperature (T_1) and highest temperature (T_n):

$$\mathbf{S}(T_i) = N_F(T_i)\, \mathbf{S}(T_1) + N_U(T_i)\, \mathbf{S}(T_n) \qquad (A2)$$

Here $N_F(T_i)$ and $N_U(T_i)$ are the fractional populations of the folded and unfolded species, respectively. By substituting eq A1 into eq A2, we obtain

$$N_F(T_i) = \frac{c_2(T_n) - c_2(T_i)}{c_2(T_n) - c_2(T_1)} \qquad (A3)$$

which is the normalized second SVD coefficient. Therefore, approximate values of the enthalpy and entropy of denaturation can be obtained by fitting the equilibrium constant from the second SVD component ($K = N_U/N_F$) to $RT \log K = -\Delta H + T\Delta S$.

When the measured signal is not linearly proportional to concentration, as is the case for background-free (homodyne) nonlinear experiments such as the DVE, the above relation does not generally hold but is valid when spectral changes with temperature are small. From eq 7, we define

$$\mathbf{S}_{DVE} = |\mathbf{S}_E|^2 \propto \left| \int_{-\infty}^{\infty} \mathbf{S}_C(\omega_1, \tau_2, \omega_3)\, d\omega_1 \right|^2 \qquad (A4)$$

where $\mathbf{S}_E$ is the 2D correlation spectrum integrated over ω_1. Because $\mathbf{S}_E$ is linear in concentration and $N_F(T_i) + N_U(T_i) = 1$,

$$\mathbf{S_E}(T_i) = N_F(T_i)\,\mathbf{S_E}(T_1) + N_U(T_i)\,\mathbf{S_E}(T_n) =$$
$$\mathbf{S_E}(T_1) + N_U(T_i)\,\Delta\mathbf{S_E} \quad (A5)$$

where $\Delta\mathbf{S_E}$ is the difference spectra between the lowest and highest temperature. In the limit that $|\Delta\mathbf{S_E}| \ll |\mathbf{S_E}|$, we obtain the same linear equation for the temperature-dependent changes to the DVE spectrum using population conservation ($N_F(T_i) + N_U(T_i) = 1$) and eq A5:

$$\mathbf{S_{DVE}}(T_i) = \mathbf{S_{DVE}}(T_1) + 2N_U(T_i)\,\mathrm{Re}[\mathbf{S_E}(T_1)\cdot\Delta\mathbf{S_E}^*] +$$
$$N_U(T_i)^2|\Delta\mathbf{S_E}|^2$$
$$= N_F(T_i)\,\mathbf{S_{DVE}}(T_1) + N_U(T_i)\,\mathbf{S_{DVE}}(T_n) +$$
$$(N_U(T_i)^2 - N_U(T_i))|\Delta\mathbf{S_E}|^2 \quad (A6)$$
$$\approx N_F(T_i)\,\mathbf{S_{DVE}}(T_1) + N_U(T_i)\,\mathbf{S_{DVE}}(T_n)$$

Here the small third term that is ignored in the second line is incorporated in the third component of SVD analysis.

References and Notes

(1) Creighton, T. E. *Biochem. J.* **1990**, *270*, 1.

(2) Dobson, C. M.; Sali, A.; Karplus, M. *Angew. Chem., Int. Ed.* **1998**, *37*, 868.

(3) Eaton, W. A.; Muñoz, V.; Hagen, S. J.; Jas, G. S.; Lapidus, L. J.; Henry, E. R.; Hofrichter, J. *Annu. Rev. Biophys. Biomol. Struct.* **2000**, *29*, 327.

(4) Gruebele, M. *Annu. Rev. Phys. Chem.* **1999**, *50*, 485.

(5) Balbach, J.; Forge, V.; Lau, W. S.; van Nuland, N. A. J.; Brew, K.; Dobson, C. M. *Science* **1996**, *274*, 1161.

(6) Schotte, F.; Lim, M.; Jackson, T. A.; Smirnov, A. V.; Soman, J.; Olson, J. S.; Jr., P. G. N.; Wulff, M.; Anfinrud, P. A. *Science* **2003**, *300*, 1944.

(7) Perman, B.; Srajer, V.; Ren, Z.; Teng, T.-y.; Pradervand, C.; Ursby, T.; Bourgeois, D.; Schotte, F.; Wulff, M.; Kort, R.; Hellingwerf, K.; Moffat, K. *Science* **1998**, *279*, 1946.

(8) Doniach, S. *Chem. Rev.* **2001**, *101*, 1763.

(9) Gruebele, M.; Sabelko, J.; Ballew, R.; Ervin, J. *Acc. Chem. Res.* **1998**, *31*, 699.

(10) Eaton, W. A.; Muñoz, V.; Thompson, P. A.; Henry, E. R.; Hofrichter, J. *Acc. Chem. Res.* **1998**, *31*, 745.

(11) Dyer, R. B.; Gai, F.; Woodruff, W. H.; Gilmanshin, R.; Callender, R. H. *Acc. Chem. Res.* **1998**, *31*, 709.

(12) Bredenbeck, J.; Helbing, J.; Sieg, A.; Schrader, T.; Zinth, W.; Renner, C.; Behrendt, R.; Moroder, L.; Wachtveitl, J.; Hamm, P. *Proc. Natl. Acad. Sci. U.S.A.* **2003**, *100*, 6452.

(13) Bredenbeck, J.; Helbing, J.; Behrendt, R.; Renner, C.; Moroder, L.; Wachtveitl, J.; Hamm, P. *J. Phys. Chem. B* **2003**, *107*, 8654.

(14) Yamamoto, K.; Mizutani, Y.; Kitagawa, T. *Biophys. J* **2000**, *79*, 485.

(15) Goldbeck, R. A.; Thomas, Y. G.; Chen, E.; Esquerra, R. M.; Kliger, D. S. *Proc. Natl. Acad. Sci. U.S.A.* **1999**, *96*, 2782.

(16) O'Connor, D. B.; Goldbeck, R. A.; Hazzard, J. H.; Kliger, D. S.; Cusanovich, M. A. *Biophys. J.* **1993**, *65*, 1718.

(17) Chen, E.; Wittung-Stafshede, P.; Kliger, D. S. *J. Am. Chem. Soc.* **1999**, *121*, 3811.

(18) Xie, X.; Simon, J. D. *Rev. Sci. Instrum.* **1989**, *60*, 2614.

(19) Chen, E.; Goldbeck, R. A.; Kliger, D. S. *J. Phys. Chem. A* **2003**, *107*, 8149.

(20) Lewis, J.; Goldbeck, R. A.; Kliger, D. S.; Xie, X.; Dunn, R. C.; Simon, J. D. *J. Phys. Chem.* **1992**, *96*, 5243.

(21) Torii, H.; Tasumi, M. *J. Chem. Phys.* **1992**, *96*, 3379.

(22) Krimm, S.; Bandekar, J. *Adv. Protein Chem.* **1986**, *38*, 181.

(23) Hamm, P.; Lim, M.; DeGrado, W. F.; Hochstrasser, R. M. *Proc. Natl. Acad. Sci. U.S.A.* **1999**, *96*, 2036.

(24) Woutersen, S.; Mu, Y.; Stock, G.; Hamm, P. *Proc. Natl. Acad. Sci. U.S.A.* **2001**, *98*, 11254.

(25) Zanni, M. T.; Gnanakaran, S.; Stenger, J.; Hochstrasser, R. M. *J. Phys. Chem. B* **2001**, *105*, 6520.

(26) Woutersen, S.; Hamm, P. *J. Phys.: Condens. Matter* **2002**, *14*, R1035.

(27) Huang, R.; Kubelka, J.; Barber-Armstrong, W.; Silva, R. A. G. D.; Decatur, S. M.; Keiderling, T. A. *J. Am. Chem. Soc.* **2004**, *126*, 2346.

(28) Moran, A.; Mukamel, S. *Proc. Natl. Acad. Sci. U.S.A.* **2004**, *101*, 506.

(29) Cha, S.; Ham, S.; Cho, M. *J. Chem. Phys.* **2002**, *117*, 740.

(30) Ham, S.; Cho, M. *J. Chem. Phys.* **2003**, *118*, 6915.

(31) Khalil, M.; Demirdöven, N.; Tokmakoff, A. *J. Phys. Chem. A* **2003**, *107*, 5258.

(32) Zanni, M. T.; Hochstrasser, R. M. *Curr. Opin. Struct. Biol.* **2001**, *11*, 516.

(33) Demirdöven, N.; Khalil, M.; Golonzka, O.; Tokmakoff, A. *J. Phys. Chem. A* **2001**, *105*, 8025.

(34) Thompson, D. E.; Merchant, K. A.; Fayer, M. D. *J. Chem. Phys.* **2001**, *115*, 317.

(35) Merchant, K. A.; Xu, Q.-H.; Thompson, D. E.; Fayer, M. D. *J. Phys. Chem. A* **2002**, *106*, 8839.

(36) Choi, J.-H.; Ham, S.; Cho, M. *J. Phys. Chem. B* **2003**, *107*, 9132.

(37) Torii, H.; Tasumi, M. *J. Raman Spectrosc.* **1998**, *29*, 81.

(38) Woutersen, S.; Hamm, P. *J. Phys. Chem. B* **2000**, *104*, 11316.

(39) Woutersen, S.; Hamm, P. *J. Chem. Phys.* **2001**, *115*, 7737.

(40) Hamm, P.; Lim, M.; Hochstrasser, R. M. *J. Phys. Chem. B* **1998**, *102*, 6123.

(41) Barth, A.; Zscherp, C. *Q. Rev. Biophys.* **2002**, *35*, 369.

(42) Choi, J. H.; Ham, S.; Cho, M. *J. Chem. Phys.* **2002**, *117*, 6821.

(43) Bandekar, J.; Krimm, S. *Biopolymers* **1988**, *27*, 909.

(44) Susi, H.; Byler, D. M. *Biochem. Biophys. Res. Commun.* **1983**, *115*, 391.

(45) Byler, D. M.; Susi, H. *Biopolymers* **1986**, *25*, 469.

(46) Dong, A.; Huang, P.; Caughey, W. S. *Biochemistry* **1990**, *29*, 3303.

(47) Cheatum, C. M.; Tokmakoff, A.; Knoester, J. *J. Chem. Phys.* **2004**, *120*, 8201.

(48) Demirdöven, N.; Cheatum, C. M.; Chung, H. S.; Khalil, M.; Knoester, J.; Tokmakoff, A. *J. Am. Chem. Soc.* **2004**, *126*, 7981.

(49) Miyazawa, T.; Blout, E. R. *J. Am. Chem. Soc.* **1961**, *83*, 712.

(50) Wlodawer, A.; Svensson, L. A.; Sjolin, L.; Gilliland, G. L. *Biochemistry* **1988**, *27*, 2705.

(51) Santoro, J.; Gonzalez, C.; Marta, B.; Neira, J. L.; Nieto, J. L.; Herranz, J.; Rico, M. *J. Mol. Biol.* **1993**, *229*, 722.

(52) Stelea, S. D.; Pancoska, P.; Benight, A. S.; Keiderling, T. A. *Protein Sci.* **2001**, *10*, 970.

(53) Reinstädler, D.; Fabian, H.; Backmann, J.; Naumann, D. *Biochemistry* **1996**, *35*, 15822.

(54) Chen, M. C.; Lord, R. C. *Biochemistry* **1976**, *15*, 1889.

(55) Takeda, N.; Kato, M.; Taniguchi, Y. *Biochemistry* **1995**, *34*, 5980.

(56) Hermans, J.; Scheraga, H. A. *J. Am. Chem. Soc.* **1961**, *83*, 3283.

(57) Matheson, R. R.; Scheraga, H. A. *Biochemistry* **1979**, *18*, 2437.

(58) Matthews, C. R.; Froebe, C. L. *Macromolecules* **1981**, *14*, 452.

(59) Seshadri, S.; Oberg, K. A.; Fink, A. L. *Biochemistry* **1994**, *33*, 1351.

(60) Klink, T. A.; Woycechowsky, K. J.; Taylor, K. M.; Raines, R. T. *Eur. J. Biochem.* **2000**, *267*, 567.

(61) Sosnick, T. R.; Trewhella, J. *Biochemistry* **1992**, *31*, 8329.

(62) Fabian, H.; Mantsch, H. H. *Biochemistry* **1995**, *34*, 13651.

(63) Sung, J.; Silbey, R. J. *J. Chem. Phys.* **2001**, *115*, 9266.

(64) Khalil, M.; Demirdöven, N.; Tokmakoff, A. *Phys. Rev. Lett.* **2003**, *90*, 47401.

(65) Gallagher Faeder, S. M.; Jonas, D. M. *J. Phys. Chem. A* **1999**, *103*, 10489.

(66) Jackson, M.; Mantsch, H. H. *Crit. Rev. Biochem. Mol. Biol.* **1995**, *30*, 95.

(67) Shrager, R. I.; Hendler, R. W. *Anal. Chem.* **1982**, *54*, 1147.

(68) Hofrichter, J.; Henry, E. R.; Sommer, J. H.; Deutsch, R.; Ikeda-Saito, M.; Yonetani, T.; Eaton, W. A. *Biochemistry* **1985**, *24*, 2667.

(69) Chen, W.-G.; Braiman, M. S. *Photochem. Photobiol.* **1991**, *54*, 905.

(70) Makhatadze, G. I.; Privalov, P. L. *Adv. Protein Chem.* **1995**, *47*, 307.

(71) Pace, C. N.; Grimsley, G. R.; Thomas, S. T.; Makhatadze, G. I. *Protein Sci.* **1999**, *8*, 1500.

(72) Scheurer, C.; Piryatinski, A.; Mukamel, S. *J. Am. Chem. Soc.* **2001**, *123*, 3114.

(73) Woutersen, S.; Pfister, R.; Hamm, P.; Mu, Y. G.; Kosov, D. S.; Stock, G. *J. Chem. Phys.* **2002**, *117*, 6833.